HYDRODYNAMIC IMPELLER STIFFNESS, DAMPING, AND INERTIA IN THE ROTORDYNAMICS OF CENTRIFUGAL FLOW PUMPS

B. Jery, A. J. Acosta, C. E. Brennen, and T. K. Caughey
California Institute of Technology
Pasadena, California 91125

Measurements were made of the lateral hydrodynamic forces experienced by a centrifugal pump impeller performing circular whirl motions within several volute geometries. Experiments were conducted for various flow coefficients, ϕ, impeller rotating speeds or angular frequencies, ω, and the angular frequency of the whirl motion, Ω, was varied from zero to nearly synchronous ($\Omega=\omega$) and to nearly anti-synchronous ($\Omega=-\omega$). The lateral forces were decomposed into (i) time averaged lateral forces and (ii) hydrodynamic force matrices representing the variation of the lateral forces with position of the impeller center. No assumptions concerning the form of these matrices need to be made. The latter can be further decomposed according to the variation with whirl frequency, the result being "stiffness", "damping", and "fluid inertial" rotordynamic force matrices. It was found that these force matrices essentially consist of equal diagonal terms and skew-symmetric off-diagonal terms. One consequence of this is that during its whirl motion the impeller experiences forces acting normal and tangential to the locus of whirl. Data on these normal and tangential forces are presented; in particular it is shown that there exists a region of positive reduced whirl frequencies, Ω/ω, within which the hydrodynamic forces can be destabilizing with respect to whirl.

NOMENCLATURE

$[A]$ = dimensionless hydrodynamic force matrix

$[B]$ = the 6X6 internal balance calibration matrix

$[C]$ = hydrodynamic damping matrix as defined by Eq.(3).

b_2 = impeller discharge width

* The authors are indebted to the NASA George Marshall Space Flight Center, Huntsville, Alabama for their continued sponsorship of this research under contract NAS8-33108. We are also most grateful for the help given by graduate students D. Adkins and R. Franz and undergraduates W. Goda and S. Moriarty. One of the authors (B.J.) would also like to thank Byron-Jackson Pump Division, Borg-Warner Industrial Products, Inc. for financial support.

$\{F\}$ = 6-component generalized force vector

F_1, F_2 = components of instantaneous lateral force on impeller in the rotating internal balance reference frame

F_x, F_y = components of instantaneous lateral force on impeller in fixed laboratory reference frame (X,Y) non-dimensionalized by $\frac{1}{2}\rho\pi r_2^3\omega^2 b_2$

F_{ox}, F_{oy} = values of F_x and F_y when impeller axis remains coincident with the origin of the (X,Y) coordinate system

F_N, F_T = Components of instantaneous lateral force on impeller normal to and tangential to the whirl orbit, non-dimensionalized by $\frac{1}{2}\rho\pi r_2^2\omega^2 b_2\varepsilon$

I,J = integers such that $\Omega = I\omega/J$

[K] = hydrodynamic stiffness matrix as defined by Eq. (3)

[M] = hydrodynamic inertial matrix as defined by Eq. (3)

N = pump rpm = $60\omega/2\pi$

r_2 = impeller discharge radius

t = time

$\{V\}$ = 6-component vector of internal balance bridge output voltages

(X,Y) = fixed laboratory reference frame

x,y = instantaneous coordinates of impeller center in fixed laboratory reference frame (X,Y), non-dimensionalized by r_2

$\dot{x},\dot{y},\ddot{x},\ddot{y}$ = first and second time derivatives of impeller position non-dimensionalized using the distance r_2 and the time ω^{-1}

ε = radius of circular whirl orbit

ρ = density of water

ϕ = pump flow coefficient based on impeller discharge area and tip speed

Ψ = pump total head coefficient = total head rise divided by $\rho r_2^2\omega^2$

ω = radian frequency of pump shaft rotation

Ω = radian frequency of whirl motion = $I\omega/J$

Additional subscripts P and Q and superscript k refer to the Fourier decomposition of F_1 and F_2 defined in Eq. (7).

INTRODUCTION

In recent years it has been increasingly recognized that hydrodynamic cross-coupling forces can cause serious rotor dynamic problems in high speed turbomachines. Such problems have been experienced not only in steam turbines (Refs.1,2), but also in large compressors (Refs.3,4), in turbines (Ref.5) and in high speed pumps (Ref.6). Though other instability mechanisms such as internal damping or non-isotropic shaft stiffness or rotor inertia can be fairly readily characterized the same cannot be said of the hydrodynamic cross-coupling forces. Various hydrodynamic flows have been identified as possible contributors to these destabilizing forces. Bearings and particularly seals can clearly play such a role as the papers in this workshop (and previous workshops in the same series) attest. But much less is known about the potential for destabilizing forces arising from the flows associated with the impeller and diffuser of a compressor or pump; this paper will be confined to this issue.

Consider the hydrodynamic forces acting on a pump impeller in the plane perpendicular to the axis of rotation, the so-called lateral hydrodynamic forces. For present purposes a set of axes, X,Y in this plane are defined as fixed in the laboratory or "volute" frame. The origin of these axes corresponds to the design position for the axis of rotation of the impeller (impeller center) for that impeller/volute combination, also called the "volute center". Because of the asymmetry of most volute designs an impeller rotating with its center fixed in this coordinate frame will normally experience a steady force whose magnitude and direction will differ according to the position of the impeller center, denoted by O in Figure 1. Whether or not this force is zero when the impeller center, O, coincides with the volute center obviously depends upon the wisdom of the designer. In any case the lateral forces on the impeller for any position of the impeller can be represented by

$$\begin{Bmatrix} F_x \\ F_y \end{Bmatrix} = \begin{Bmatrix} F_{ox} \\ F_{oy} \end{Bmatrix} + [A] \begin{Bmatrix} x \\ y \end{Bmatrix} \tag{1}$$

In both this equation and all the equations and results which follow dimensionless forces and deflections are used (see Nomenclature for definitions). Equation (1) implicitly assumes small offsets x,y in the impeller center so that the force variations can be represented by such a linear equation (at the present time little is known of possible non-linear effects). It follows that the steady lateral forces F_x, F_y due to a fixed offset of the impeller center can be represented by the forces F_{ox}, F_{oy} generated when the impeller center coincides with the volute center (or at least some fixed laboratory position) plus a "stiffness" matrix [A]. Both will be functions of the flow conditions as represented by the flow coefficient ϕ.

A substantial body of data now exists on the lateral forces F_{ox},F_{oy} thanks to the work of Domm and Hergt (Ref.7), Agostonelli et al (Ref.8) and Iverson et al (Ref.9) among others. The present program of research at Caltech began with measurements of both the lateral forces F_{ox},F_{oy} and the hydrodynamic "stiffness" matrices [A]. This information, some of which was presented at the last workshop has been reported in Refs.10-13 and will not be repeated here. It was obtained by very slowly moving the impeller center around a circular orbit (as shown in Figure 1) and measuring the lateral forces at each location. One of the most significant features of the results is best illustrated by evaluating the forces components F_N, F_T normal and tangential to the orbit of this very slow whirl motion. It transpired that the hydrodynamic forces give rise to a positive tangential force in

the same direction as the direction of impeller rotation which would be rotordynamically destabilizing.

The present paper extends these results to the case of non-negligible velocity of the orbiting motion. Specifically a whirl motion with a circular orbit and an angular frequency, Ω, is imposed on the impeller and resulting unsteady forces are measured. Denoting the orbit radius by ε this implies that $x = \varepsilon \cos \Omega t/r_2$; $y = \varepsilon \sin \Omega t/r_2$ and that Equation (1) needs to be generalized to the form:

$$\begin{Bmatrix} F_x(t) \\ F_y(t) \end{Bmatrix} = \begin{Bmatrix} F_{ox} \\ F_{oy} \end{Bmatrix} + \frac{\varepsilon}{r_2} \left[A(\Omega/\omega)\right] \begin{Bmatrix} \cos \Omega t \\ \sin \Omega t \end{Bmatrix} \tag{2}$$

where the rotordynamic force matrix $[A(\Omega/\omega)]$ is now a function of the ratio of whirl frequency to impeller rotating frequency Ω/ω as well as the flow coefficient. On the other hand the matrices required for input into most rotordynamic analysis are the stiffness, [K], damping, [C], and inertial, [M], matrices defined by the dimensionless matrix equation

$$\begin{Bmatrix} F_x \\ F_y \end{Bmatrix} = - [M] \begin{Bmatrix} \ddot{x} \\ \ddot{y} \end{Bmatrix} - [C] \begin{Bmatrix} \dot{x} \\ \dot{y} \end{Bmatrix} - [K] \begin{Bmatrix} x \\ y \end{Bmatrix} \tag{3}$$

It follows by comparing the definitions (2) and (3) that

$$\begin{aligned} A_{xx} &= M_{xx} \frac{\Omega^2}{\omega^2} - C_{xy} \frac{\Omega}{\omega} - K_{xx} \\ A_{xy} &= M_{xy} \frac{\Omega^2}{\omega^2} + C_{xx} \frac{\Omega}{\omega} - K_{xy} \\ A_{yx} &= M_{yx} \frac{\Omega^2}{\omega^2} - C_{yy} \frac{\Omega}{\omega} - K_{yx} \\ A_{yy} &= M_{yy} \frac{\Omega^2}{\omega^2} + C_{yx} \frac{\Omega}{\omega} - K_{yy} \end{aligned} \tag{4}$$

It should be observed that Equation (3) makes the a priori assumption that the matrix [A] varies quadratically with Ω/ω. There is no fundamental reason why the hydrodynamic forces should follow such a simple behavior. Nevertheless the results of the present study do seem to be well represented by quadratics and values of [M], [C] and [K] evaluated from least squares fits to the $[A(\Omega/\omega)]$ data are presented later. Finally we note that the imposition of a circular orbit motion is analogous to performing a forced vibration experiment in a mechanical system; data are thereby extracted which have use in a more general dynamic analysis of the system.

EXPERIMENTAL FACILITY

The facility used to conduct the present experiments has been described in detail elsewhere (Refs.10,11,12,14). Only a brief description will be given here; modifications made for the purpose of the present experiments will be given more

attention. The site of the experiments is a pump loop (Figure 2) containing flow control and measuring systems. Installed in the lower left hand corner of this loop is the test pump and drive system known as the Rotor Force Test Facility (RFTF) shown schematically in Figure 3. The flow enters the centrifugal impeller (5) from the inlet connection (3) and inlet bell (4). Volutes (2) of various geometries are contained in the pump housing (1) so that the volutes can be of lightweight construction (most are made of fiberglass). The impeller (5) is mounted directly on the internal force balance (6) which is new to the present experiments and is discussed more fully below. Face seals on both the inlet and discharge side of the impeller are backed-off to prescribed clearances in order to minimize their contribution to the force on the impeller. The main pump shaft (10) rotates in a double bearing system (7,8,11) designed so that rotation of the sprocket (9) attached to the intermediate bearing cartridge causes the orbiting motion. The radius of the orbiting motion is set at 0.126cm for all of the present experiments. This motion is driven by the eccentric drive motor (2 H.P.) The main shaft is driven by the main drive motor (20 H.P.) through a gear box and a flexible shaft system designed to accommodate the whirl motion. The maximum speed of the main shaft is about 3600 rpm (Ω = 60Hz) though the current experiments have been performed at 1000 and 2000 rpm (ω = 16.7 and 33.3Hz). For reasons discussed below the whirl speed is presently limited to 1000 rpm.

Previous measurements of the steady forces at zero whirl frequency (Ref.10,11,12,13) were made using an external force balance whose operation required floating the entire bearing system and measuring the forces on this floating mass. Though simpler to implement, this external balance system was severely limited in its dynamic capability. The internal balance was designed to measure the unsteady forces implicit in the case of non-zero whirl frequencies (as well as other unsteady forces such as caused by rotor/stator blade interactions though these are not addressed in the present paper). It is also designed to measure all 6 components of force and moment experienced by the impeller. The design of the internal balance is shown in the schematic of Figure 4. Essentially, it consists of four equally spaced "posts" parallel to the axis which connect two substantial end plates one of which is rigidly connected to the drive shaft and the other is used as a mounting base for the impeller. The four "posts" which are 2.54 cm long and have a square cross-section of 0.51cm on a side are placed at a radius of 4.76 cm. The posts and rigid end plates were machined monolithically from stainless steel. Semi-conductor strain gauges were bonded to all four faces of each post at locations indicated in Figure 4 (1/4, 1/2 and 3/4 span points). Different combinations of strain gauges were wired into bridges, designed so as to be sensitive to each of the six components of force (or force and moment components) experienced by the balance. This balance was designed to have high natural frequencies both for torsional and lateral deflections and yet be sufficiently sensitive to the forces it is intended to measure. Both the torsional and lateral natural frequencies with the impeller attached to the "free" end plate were estimated to be about 480 Hz. However Fourier analysis of the spectrum of natural frequencies when the balance was installed indicated a considerably lower natural frequency of about 160 Hz (see Figure 5). The additional flexibility is attributed to the shaft and the bearing system. Structurally the balance was completed by a waterproof shield enveloping the two end plates. The internal air pressure was maintained at a constant, regulated value using the hole through the center of the shaft and a pneumatic collar connecting this with an exterior air supply. The wires from the strain gauges were led through the same hollow shaft and connected to a set of 52 slip rings. For the purpose of the analysis discussed below it should be noted that the lateral forces F_1, F_2 registered by the impeller

are in a frame of reference rotating and whirling with the impeller.

Unsteady fluid flow measurements such as those attempted here require sufficient control to permit data to be taken over many cycles of both the whirl and main shaft frequencies. This demands close control of both motions which was achieved by means of the control system shown diagrammatically in Figure 6. A single frequency generator feeds a frequency multiplier/divider utilizing the input of two integers I,J chosen by the operator. One output signal at a frequency ω drives the main shaft motor, a feedback control system ensuring close adherence to that driving signal. Another output at a frequency $\Omega = I\omega/J$ controls the eccentric drive motor which is also provided with a feedback control system. Three other outputs from the frequency multiplier/divider at frequencies of $\omega \pm \Omega$ or $(J \pm I)\omega/J$ and ω/J are used in the data acquisition and processing systems. The flow fluctuator control system which is also shown in Figure 6 has not as yet been used in the research program.

The central component of the signal processing system is a 16-channel digital signal processor which utilizes a reference frequency (ω, $\Omega = I\omega/J$, ω/J or $\omega \pm \Omega$) and accumulates an "average cycle" of data for each of the 16 data input channels, described by 64 digital values per cycle per channel. This data is accumulated for up to 4096 reference cycles. Subsequent Fourier analysis of this digital data evaluates not only the magnitude and phase of the fundamental present in each data channel but also the same information for many higher harmonics. In the present experiments the lowest common frequency ω/J, was used as the reference frequency; thus the Jth harmonic yields the magnitude and phase (or in-phase and quadrature components) of the component of the measurement at the main shaft frequency and the Ith harmonic does likewise for the component at the whirl frequency. (The importance of the control system described earlier in which integer values for I and J are chosen by the operator should now be apparent.) The present paper concentrates on the results obtained for the impeller forces as measured by the internal balance. Since this is <u>rotating</u> with the impeller it follows that the primary results of interest follow from the Jth, $|J-I|$th and $|J+I|$th harmonics (see below). Auxiliary information on flow rates, pressures, etc was obtained in the same way as reported in Ref.10,11,12 and 13.

INTERNAL BALANCE CALIBRATION

As discussed above the internal balance includes nine full Wheatstone bridges each of which is primarily sensitive to one or two of the force and moment components. Six of these nine bridges were selected to sense the six components, the other three being monitored as a back-up check on the main measurements. The purpose of the calibration procedure was to produce a 6X6 calibration matrix, [B], which would include all of the possible balance interactions so that the six component vector of forces {F} could be subsequently calculated from the six component vector of output voltages {V} by

$$\{F\} = [B]\ \{V\} \tag{5}$$

A number of different calibrations, hysteresis tests and dynamic response tests were performed on the balance in situ. The basic calibration matrix was obtained by in situ static loading of the balance using wires, pulleys and weights. The resulting 36 graphs displayed satisfactory linearity in both the principal and interaction

matrix elements. One of the principal element calibrations is shown in Figure 7. The largest interactions occurred in the thrust measuring bridge and these were less than 5% of the principal element outputs. The interactions in the lateral force bridges was of the order of 1%. Hysteresis tests performed by fairly rapid manual operation of the static calibration system revealed virtually no significant hysteretic effects.

Further static and dynamic calibration tests were carried out under rotating and whirling conditions. First a smooth flywheel with hidden and known off-balance weights was used to check the earlier static calibration by rotating in air without any whirl motion. This corresponds to a static loading in the rotating frame of the balance. Secondly the balanced impeller was rotated in air without whirl motion in order to detect the lateral force resulting from the weight of the impeller. This is seen by the balance as a dynamic load and allowed evaluation of the dynamic response of the balance up to about 50Hz. The magnitude and phase of the balance element response remained unchanged up to this frequency; phase angles for example were constant within $\pm 3^{o}$. Further dynamic checks were conducted using whirl motion in air.

LATERAL FORCE MEASUREMENT TECHNIQUE

Though the design and location of the internal balance was chosen to minimize parasitic forces, nevertheless it was necessary to subtract some inevitable tare forces from the raw data in order to extract the essential hydrodynamic forces imparted to the impeller. This was accomplished by performing four different sets of measurements for each eventual data point:

(i) The forces for the impeller run at the required speed and flow coefficient

(ii) The forces when the impeller is run in air at the same speed

(iii) The forces when experiment (i) is performed in water with the impeller removed

(iv) Experiment (iii) performed in air.

Subtracting (ii) from (i) and (iv) from (iii) removes the parasitic forces due to the impeller and shaft weight and small mass imbalances. Subtraction of these two results yields the force on the impeller and eliminates parasitic hydrodynamic forces on the exterior surface of the internal balance. Indeed it transpired that the annular gap between the exterior of the internal balance and the surrounding casing was sufficiently small ($\sim$ 0.5cm) to cause measurable hydrodynamic tare forces and matrices to be present in the data of (iii) minus (iv). Some of these data are given later.

The lateral forces detected by the internal balance are in a rotating reference frame. Denoting the lateral force components in the balance frame by F_1, F_2 (see Figure 8) it is necessary to describe how the average forces F_{ox}, F_{oy} and the elements of the hydrodynamic matrix [A] were obtained. First it is clear that F_x, F_y are related to F_1, F_2 by

$$F_x(t) = F_1(t) \cos \omega t - F_2(t) \sin \omega t$$
$$F_y(t) = F_1(t) \sin \omega t + F_2(t) \cos \omega t \tag{6}$$

As described earlier $F_1(t)$, $F_2(t)$ are Fourier analyzed using the reference frequency ω/J so that

$$F_1(t) = F_1^o + \sum_{k=1}^{\infty} \left(F_{1P}^k \sin \frac{k\omega t}{J} + F_{1Q}^k \cos \frac{k\omega t}{J} \right)$$
$$F_2(t) = F_2^o + \sum_{k=1}^{\infty} \left(F_{2P}^k \sin \frac{k\omega t}{J} + F_{2Q} \cos \frac{k\omega t}{J} \right) \tag{7}$$

and F_1^o, F_2^o, F_{1P}^k, F_{1Q}^k and F_{2Q}^k are available up to some limiting value of k from the digital data acquisition system and software. Eliminating F_1, F_2 from (6) and (7), substituting the resulting expressions for F_x, F_y into (2) and then integrating over one cycle of frequency ω/J results in the following relations

$$F_{ox} = -\tfrac{1}{2} \left(F_{2P}^J - F_{1Q}^J \right)$$

$$F_{oy} = \tfrac{1}{2} \left(F_{1P}^J + F_{2Q}^J \right)$$

$$A_{xx} = \frac{1}{2\varepsilon} \left(-F_{2P}^{J-I} + F_{1Q}^{J-I} - F_{2P}^{J+I} + F_{1Q}^{J+I} \right)$$

$$A_{xy} = \frac{1}{2\varepsilon} \left(-F_{1P}^{J-I} - F_{2Q}^{J-I} + F_{1P}^{J+I} + F_{2Q}^{J+I} \right)$$

$$A_{yx} = \frac{1}{2\varepsilon} \left(F_{1P}^{J-I} + F_{2Q}^{J-I} + F_{1P}^{J+I} + F_{2Q}^{J+I} \right)$$

$$A_{yy} = \frac{1}{2\varepsilon} \left(-F_{2P}^{J-I} + F_{1Q}^{J-I} + F_{2P}^{J+I} - F_{1Q}^{J+I} \right)$$

Thus evaluation of the Jth, (J-I)th and (J+I)th harmonics are required. The usual value chosen for J was 10 though the data points at the lowest whirl frequency used J=20,18,16,14 and 12; I ranged from -9 to +9.

Experimental Test Matrix

Altogether seven sets of measurements have been made to date. In each of these sets the whirl motion radian frequency Ω (as given by the choice of integers I and J) was varied while holding the pump speed ω, flow coefficient ϕ and the face seal clearances fixed.

All seven sets of measurements used the same five-bladed centrifugal impeller (Impeller X) which has an outer radius r_2=16.2cm and discharge angle of 25 degrees. This impeller was cast out of bronze and has a specific speed of 0.57. In five out of the seven sets a logarithmic spiral volute (Volute A) was used. This is a well-matched trapezoidal cross-section fiberglass volute that was designed to be used

with Impeller X. The ratio of the base circle diameter to impeller diameter is 1.13, and the area at the cutwater was 20.75cm^2. One set of measurements was conducted using a circular volute (Volute B), deliberately mismatched with its 5.42cm constant diameter circular cross-section. Finally, a set of measurements was made with Impeller X rotating and whirling inside the pump outer casing, in the absence of any volute.

A face-seal clearance 0.13mm was maintained throughout all the experiments. However, in one particular set of measurements two circular rings were attached to the interior of the volute on either side of the impeller discharge in order to reduce the leakage flow.

Six of the sets were conducted at 1000 rpm impeller speed, while the whirl speed was varied from 0 to 900 rpm in both directions ($-0.9 \leq \Omega/\omega \leq 0.9$). The remaining set was made at 2000 rpm to study the influence of pump speed on the hydrodynamic forces; in this case the whirl speed was varied from 0 to 1000 rpm in both directions ($-0.5 \leq \Omega/\omega \leq 0.5$). The restriction on the highest whirl speed is merely a precautionary measure to limit the inertial loads and mechanical vibrations on the eccentric drive assembly and dynamometer. The combination of Volute A and Impeller X was tested at 3 values of ϕ (.06, .092 and 0.131) and 1000 rpm pump speed. All other experiments mentioned earlier were conducted at "design" condition of $\phi = .092$.

RESULTS

The results presented in this paper will be confined to the data obtained for the hydrodynamic force matrix $[A(\Omega/\omega)]$, the associated average normal and tangential forces F_N, F_T given by

$$F_N = \frac{1}{2}(A_{xx} + A_{yy})$$

$$F_T = \frac{1}{2}(-A_{xy} + A_{yx})$$

and the stiffness, damping and inertia matrices [K], [C] and [M] as defined by Eq. (3). Other data such as the hydrodynamic performance ($\Psi(\phi)$) and the average lateral forces F_{ox}, F_{oy} will be presented in later reports. It should however be noted that the F_{ox}, F_{oy} values obtained were essentially independent of the whirl speed and agreed with those measured by Chamieh et al (Refs. 10,11,12). Thus we concentrate here on one of the results of primary importance in the rotordynamic analysis of centrifugal pumps.

The various experimental measurements are compared with a base case, namely the results for the Volute A/Impeller X combination run at 1000 rpm and the design flow coefficient ϕ of 0.092 with face seal clearances set at 0.13mm. The $[A(\Omega/\omega)]$ matrix for this case is shown in Figure 9 plotted against Ω/ω. In common with all the other cases tested this matrix has almost equal diagonal terms and off-diagonal terms which are almost equal but of opposite sign. This skew-symmetric form for the hydrodynamic matrix is remarkable since there is no fundamental reason why it should take this form. This form is often <u>assumed</u> but this is the first confirmation that we are aware of.

Because of this skew-symmetric form of the hydrodynamic force matrix it is convenient to present only the arithmetic mean of the diagonal terms which, in fact, corresponds to the dimensionless normal force, F_N, averaged over the whirl orbit and half the difference of the off-diagonal terms which in fact corresponds to the dimensionless tangential force, F_T, similarly averaged. The values of F_N, F_T corresponding to Figure 9 are shown in Figure 10. The variation in these quantities with flow coefficient and with speed are shown in Figures 11 and 12. The effect of two rings that were attached to the volute on either side of the impeller discharge in order to reduce the seal leakage is shown in Figure 13. Finally a comparison of the results for Volutes A and B is included in Figure 14.

Several general features of these results should be emphasized. Considering first F_N note that the hydrodynamic force is almost always in the radially outward direction. At zero whirl frequency it has a positive value which is in close agreement with the results of Chamieh et al (Refs. 10,11,12); this corresponds to a negative stiffness at zero whirl speed. The sign of the tangential force, F_T is such as to produce a rotordynamically stabilizing effect at negative whirl speeds and for the larger positive whirl speed. However it is important to note that there is a region of positive whirl speeds between zero and $\Omega/\omega = 0.25 \rightarrow 0.5$ in which the tangential force is destabilizing rotordynamically. It would appear from Figure 11 that this destabilizing interval increases somewhat as the flow coefficient decreases.

Conventional scaling of forces with speed in pumps would imply that the data for 1000 rpm and 2000 rpm should be identical when plotted in the chosen dimensionless form. Figure 12 demonstrates that this is the case for the normal force F_N. but the tangential force, F_T, at negative whirl speeds appears to be significantly different for these two pump speeds. This could be due to viscous, frictional forces which do not scale with the square of the velocity.

The addition of the leakage reducing rings shown in Figure 13 had little effect on the results except for F_T at negative whirl speeds.

Note that all of the F_N data in Figures 10 to 13 is essentially the same. Only when the volute is changed (Figure 14) is the normal force altered. The lower values of F_N for Volute B would be expected since it has a larger cross-sectional area. However the tangential forces were similar for the two volutes.

As an aside we included here the hydrodynamic tares caused by the flow exterior to the balance and shaft. These were earlier described as the difference in the results of experiments (iii) and (iv). Note from Figure 15 that these tares amount to about 5-10% of the measured impeller effects. However it is interesting to note that the functional form of these tare forces is similar to that for the impeller forces.

The conventional stiffness, damping and inertia matrices used by rotordynamicists were defined in Eq. (3) and (4). It is clear from Figures 9 through 14 that the data can be fairly well represented by the quadratics given in Eq. (4). Dimensionless values of [K], [C] and [M] for the various experiments are presented in Table II. The values without parentheses are the result of quadratic least squares fits to the data for both positive and negative whirl speeds. The data in parentheses are the result of quadratic least squares fits to the data for positive whirl speeds only. Discrepancies between these values are therefore a

result of a combination of deviation from the quadratic behavior and uncertainty in the matrix element values. For example it is clear that the curvature of the F_T is small and somewhat uncertain; this results in substantial discrepancies in the off-diagonal terms of the inertia matrix, [M]. On the other hand all the elements of the stiffness matrix, [K], are well defined. The latter are quite consistent with the quasi-statically measured stiffness matrices of Chamieh et al (Ref.10,11,12). The damping and inertia matrices represent new data. They can be directly compared with the matrices presented by Ohashi at this workshop. In doing so one notes that the values for all matrices are substantially larger than those of Ohashi's. Though the reasons for this are not clear at this time, it should be pointed out that the volute boundaries are much closer to the impeller in the present experiments and this should result in higher values of the damping and added mass (or inertial effects). Note for example the last line of Table II which represents values obtained in the absence of a volute (though the pressure casing is still close enough to produce a significant effect).

CONCLUSIONS

In conclusion we note that the data presented in this paper represents the first experimental measurements of the complete hydrodynamic force matrix for a whirling centrifugal pump impeller. The common assumption of skew-symmetry for these matrices is justified by the experiments and the results come close to the commonly used quadratic variation with whirl frequency. The steady forces and stiffness matrices agree with those measured by Chamieh et al (Refs.10,11,12). The damping and inertial matrices are new and the effects of these on the rotordynamics of a typical pump should be tested. Many more tests are planned with the present experimental facility including tests with other impellers, volutes (with and without diffuser vanes) under a wide variety of flow conditions. The effects of cavitation will also be examined soon.

Postscript

Some preliminary data was released in June 1983. This should now be disregarded; it is superseded by the data of the present paper.

REFERENCES

1. Alford, J. S., "Protecting Turbomachinery from Self-Excited Rotor Whirl", J. of Eng. for Power, Vol. 87, pp. 333-344, Oct. 1965.

2. Pollman, E., Schwerdtfeger, H., and Termuehlen, H., "Flow Excited Vibrations in High Pressure Turbines (Steam Whirl)", J. of Eng. for Power, Vol. 100, pp. 219-228, April 1978.

3. Thompson, W. E., "Fluid Dynamic Excitation of Centrifugal Compressor Rotor Vibrations", J. Fluid Engineering, Vol. 100, pp. 73-78, March 1978.

4. Doyle, H. E., "Field Experiences with Rotodynamic Instability in High-Performance Turbomachinery", First Workshop on Rotordynamic Instability Problems in High-Performance Turbomachinery, Texas A&M University, NASA Conf. Pub. 2133, pp. 3-13, 1980.

5. Rossi, G. and Zanetti, V. 1982. "Attempt of synthesis of radial thrust measures". Symp. on Operating Problems of Pump Stations and Power Plants, (Proc. 11th IAHR Symp. on Hydraulic Machinery, Equipment and Cavitation), Amsterdam, Netherlands, Sept. 1982, Vol.2, Paper 52.

6. Ek, M. C., "Solution of the Subsynchronous Whirl Problem in the High Pressure Hydrogen Turbomachinery of the Space Shuttle Main Engine", Paper No. 78-1002, AIAA/SAE 14th Joint Propulsion Conf., Las Vegas, Nevada, July 25-28 1978.

7. Domm, H., and Hergt, P., "Radial Forces on Impeller of Volute Casing Pumps", Flow Research on Blading (L. S. Dzung, ed.), Elsevier Pub. Co., The Netherlands, pp. 305-321, 1970.

8. Agostinelli, A., Nobles, D., and Mockridge, C. R., "An Experimental Investigation of Radial Thrust in Centrifugal Pumps", Trans. ASME, J. of Eng. for Power, Vol. 82, pp. 120-126, April 1960.

9. Iversen, H. W., Rolling, R. E., and Carlson, J. J., "Volute Pressure Distribution, Radial Force on the Impeller and Volute Mixing Losses of a Radial Flow Centrifugal Pump", Trans. ASME, J. of Eng. for Power, Vol. 82, pp. 136-144, April 1960.

10. Chamieh, D. S. "Forces on a Whirling Centrifugal Pump - Theory and Experiments", Ph. D. Thesis, Division of Engineering and Applied Science, California Institute of Technology, February 1983.

11. Chamieh, D. S., Acosta, A. J., Brennen, C. E. and Caughey, T. K. "Experimental Measurements of Hydrodynamic Radial Forces and Stiffness Matrices for a Whirling Centrifugal Pump Impeller" (Submitted to J. Fl. Eng.)

12. Chamieh, D. S., Acosta, A. J., Brennen, C. E., Caughey, T. K. and Franz, R., "Experimental Measurements of Hydrodynamic Stiffness Matrices for a Centrifugal Pump Impeller", Proceedings of NASA/ARO Workshop on Rotordynamic Instability Problems in High Performance Turbomachinery, NASA CP-2250, 1982, pp. 382-398.

13. Jery, B. and Franz, R., "Stiffness Matrices for the Rocketdyne Diffuser Volute", California Institute of Technology, Div. of Eng. and Appl. Sci., Report No. E249.1, October, 1982.

14. Brennen, C. E., Acosta, A. J. and Caughey, T. K., "A Test Program to Measure Cross-Coupling Forces in Centrifugal Pumps and Compressors", Proc. Workshop on Rotordynamic Instability Problems in High Performance Turbomachinery, Texas A&M Univ., May 1980.

TABLE I

Rotordynamic stiffness, damping and inertia matrices. Values shown without parenthesis represent quadratic fits for both positive and negative whirl speeds. Values shown in parenthesis are the corresponding fits for positive whirl speeds only.

Volute Type	Speed, N and Flow, ϕ	K_{xx} K_{yx}	K_{xy} K_{yy}	C_{xx} C_{xy}	C_{xy} C_{yy}	M_{xx} M_{yx}	M_{xy} M_{yy}
A Spiral	1000 rpm ϕ=0.06	-1.60 (-1.59)	0.80 (0.85)	2.13 (1.64)	7.08 (6.48)	6.72 (5.91)	0.12 (0.91)
		-1.03 (-1.04)	-1.46 (-1.18)	-7.13 (-5.05)	2.59 (1.63)	0.52 (-0.84)	6.61 (4.37)
A	1000 rpm ϕ=0.092	-1.43 (-1.11)	0.77 (0.72)	2.67 (1.87)	6.88 (4.95)	6.76 (4.77)	-0.10 (0.90)
		-0.84 (-0.72)	-1.42 (-1.19)	-7.06 (-5.58)	2.74 (1.52)	-0.04 (-1.45)	6.57 (5.02)
A	1000 rpm ϕ=0.131	-1.48 (-1.50)	0.82 (0.36)	4.01 (0.62)	6.35 (6.34)	6.00 (5.91)	-2.67 (1.00)
		-0.78 (-0.46)	-1.60 (-1.57)	-6.46 (-5.54)	3.77 (2.16)	1.89 (0.41)	5.91 (4.69)
A	2000 rpm ϕ=0.092	-1.88 (-2.07)	1.31 (1.20)	4.11 (2.99)	6.63 (6.82)	6.10 (4.97)	-1.04 (0.89)
		-1.45 (-1.39)	-1.80 (-2.03)	-6.53 (-7.41)	4.17 (3.23)	1.19 (-0.65)	6.30 (6.60)
A with rings	1000 rpm ϕ=0.092	-1.48 (-1.63)	0.94 (0.86)	3.92 (2.69)	6.92 (6.87)	6.71 (6.30)	-1.98 (-0.44)
		-0.97 (-0.74)	-1.48 (-1.47)	-6.87 (-6.33)	3.98 (1.80)	2.25 (-0.29)	6.12 (5.39)
B circular	1000 rpm ϕ=0.092	-1.24 (-1.40)	0.83 (0.77)	3.4 (2.18)	5.5 (5.55)	5.11 (4.80)	-1.74 (-0.15)
		-0.81 (-0.79)	-1.39 (-1.33)	-5.28 (-4.23)	3.12 (2.39)	1.34 (0.35)	4.56 (3.25)
No volute	1000 rpm ϕ=0.092	-0.32 (-0.37)	0.44 (0.75)	2.1 (2.34)	2.9 (2.04)	4.41 (3.08)	-0.31 (0.08)
		-0.39 (-0.73)	-0.22 (-0.06)	-3.03 (-0.23)	1.9 (2.18)	0.54 (0.15)	4.21 (0.64)

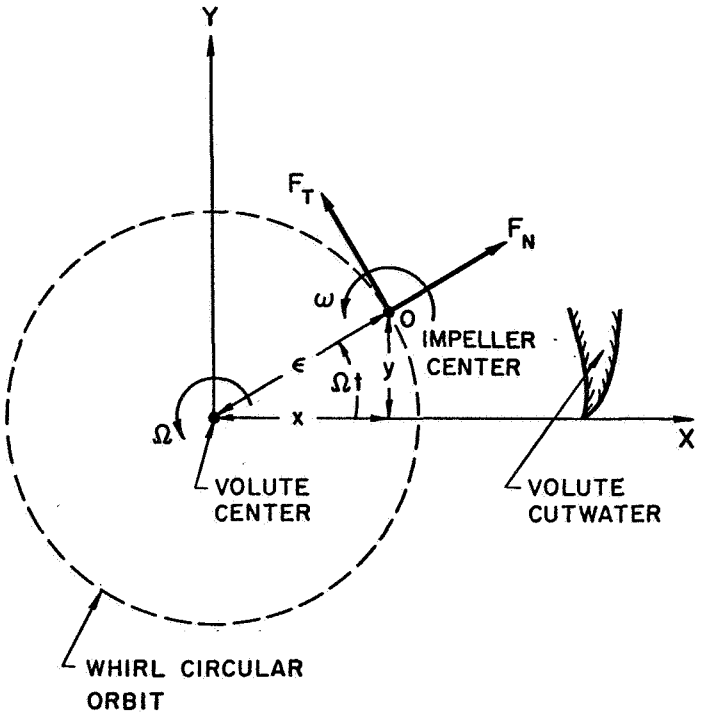

Figure 1. Coordinate system and force notation in a plane perpendicular to the axis of rotation of the impeller.

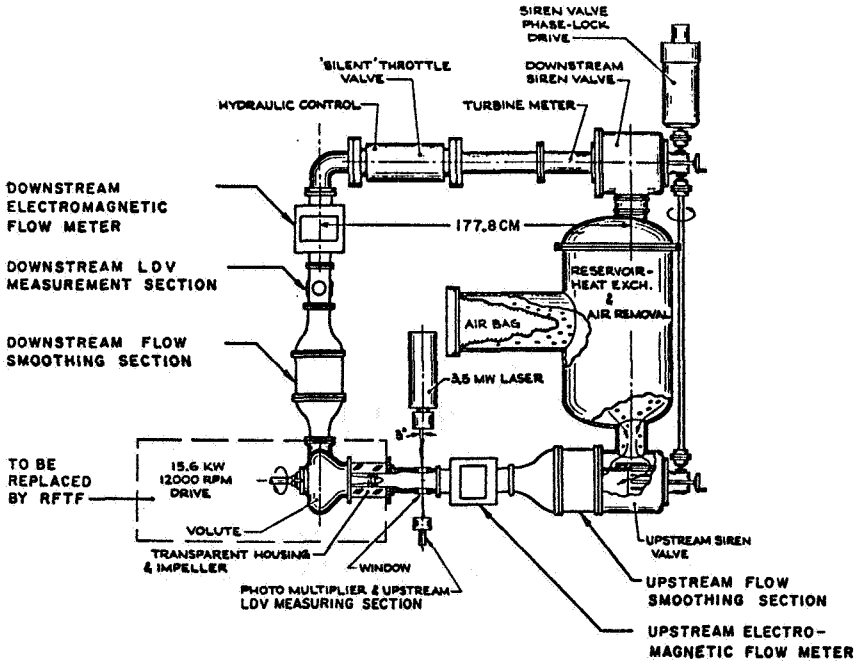

Figure 2. Schematic plan view of the pump loop prior to installation of the Rotor Force Test Facility (RFTF).

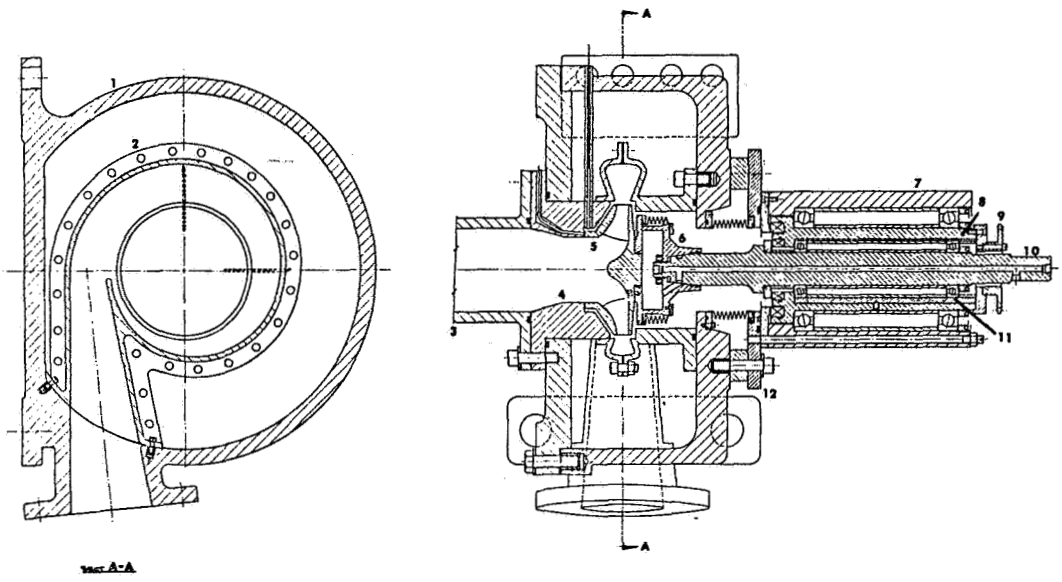

Figure 3. Cross-section of the main structure of the Rotor Force Test Facility (see text for numbered components).

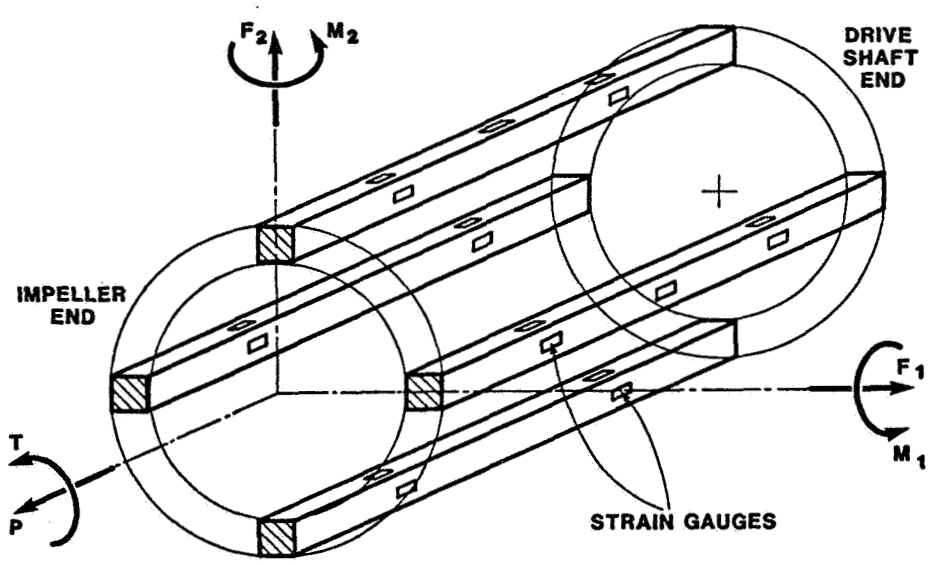

Figure 4. Schematic of the internal force balance.

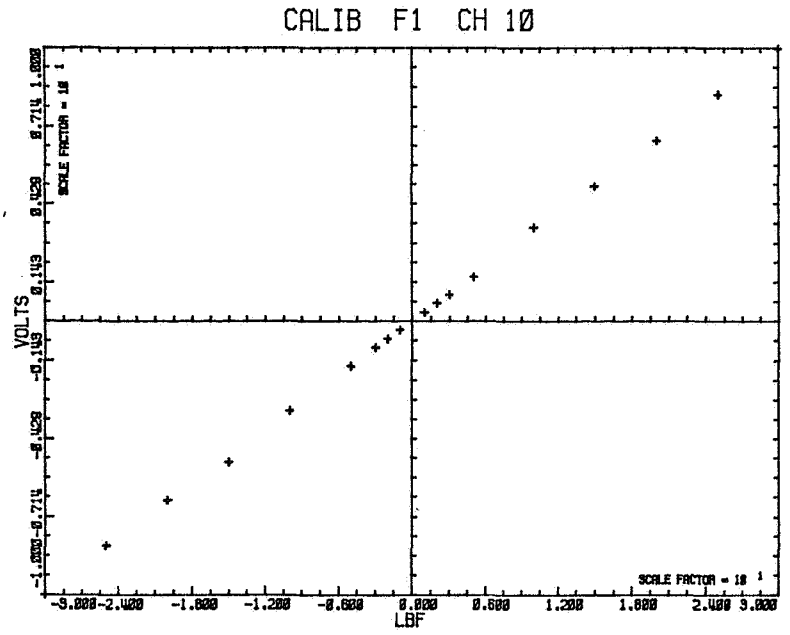

Figure 7. Typical in situ static calibration curve showing the voltage output of a principal bridge for various F_1 lateral loadings. Typical interaction outputs were also linear but only 1→2 percent of the principal outputs.

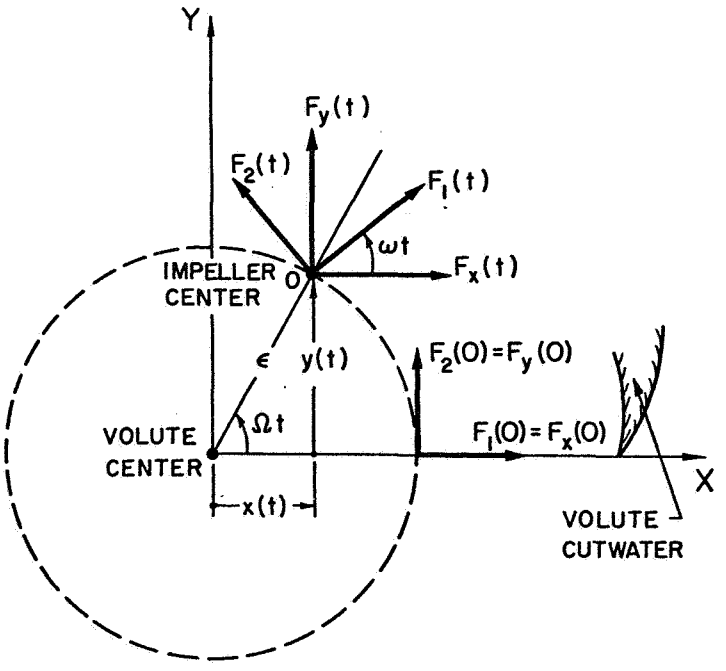

Figure 8. Schematic showing the relation between the lateral forces in the stationary X,Y frame and the rotating frame of the balance.

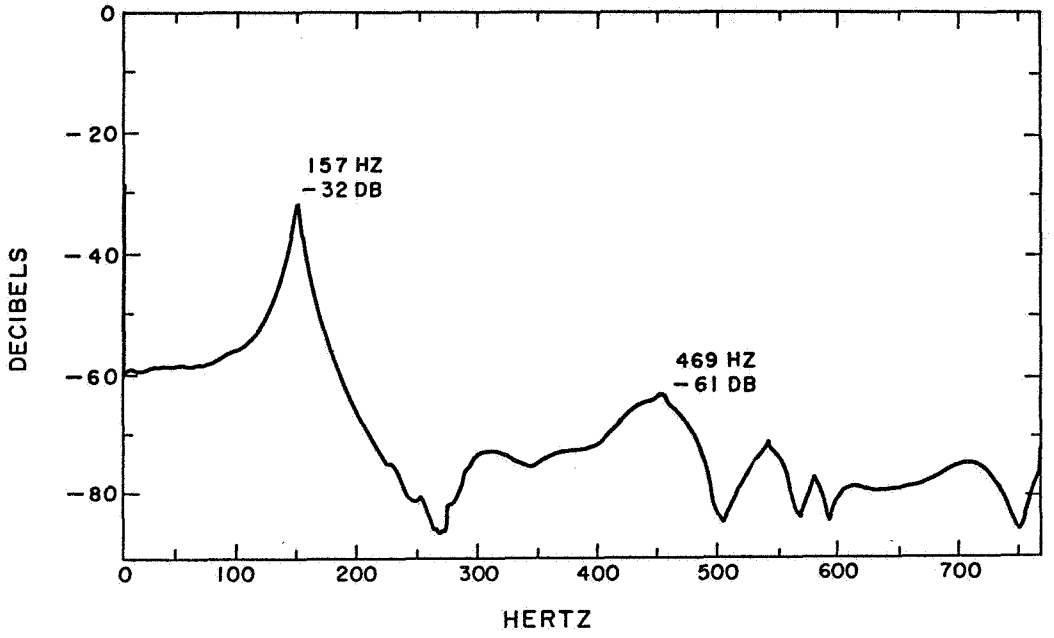

Figure 5. Frequency analysis of the installed impeller/internal balance/shaft/eccentric drive system when a lateral impulse is applied to the impeller.

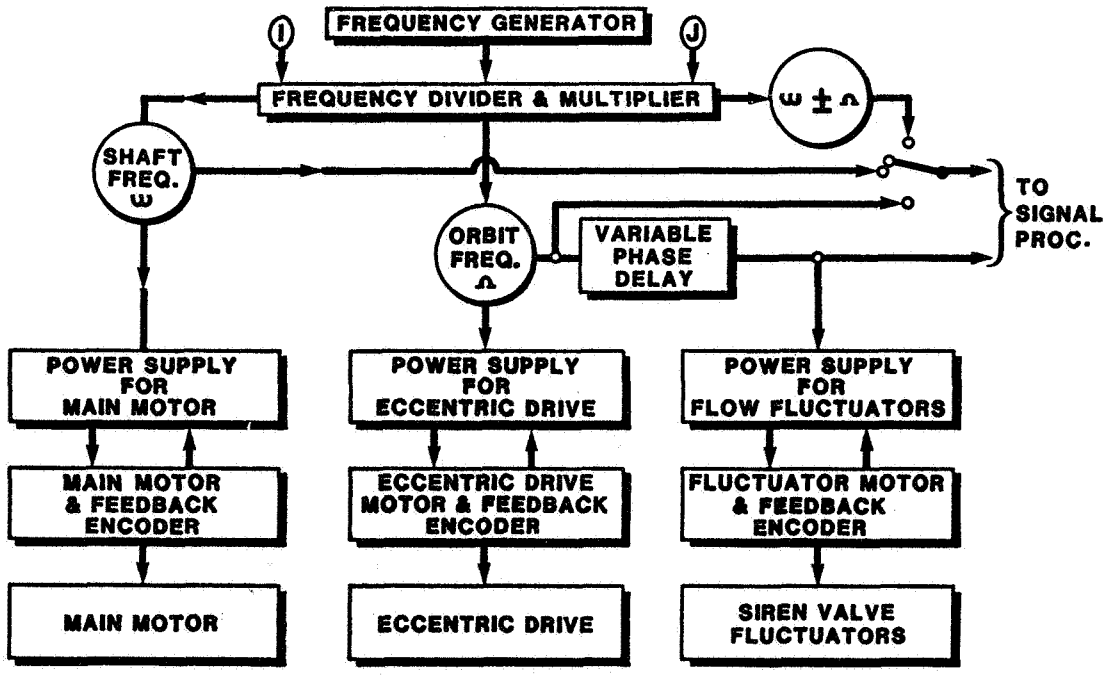

Figure 6. Schematic of the control system for the Rotor Force Test Facility.

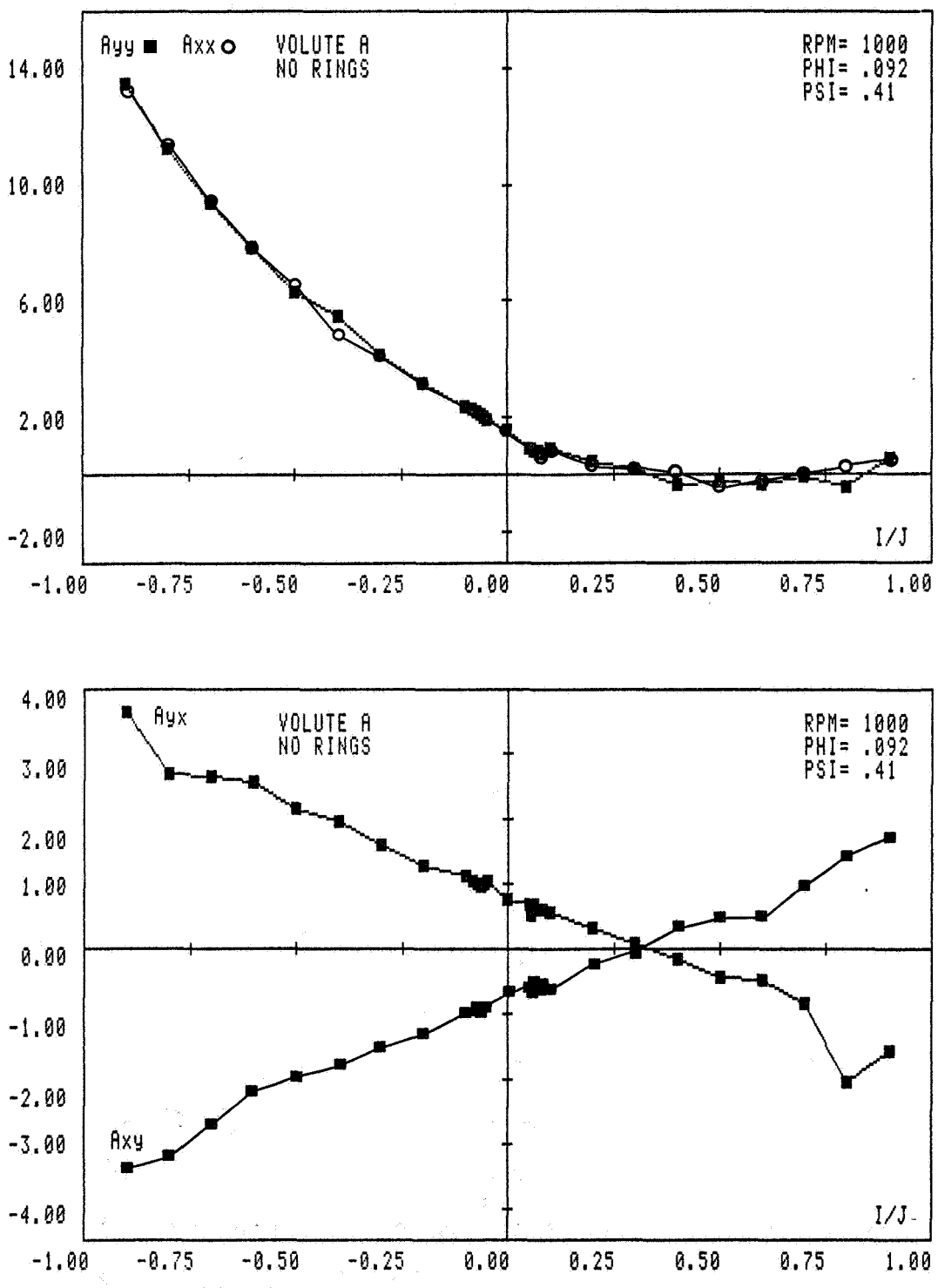

Figure 9. The hydrodynamic force matrix, [A] as a function of Ω/ω for the Volute A/Impeller X combination at 1000 rpm and ϕ = 0.092.

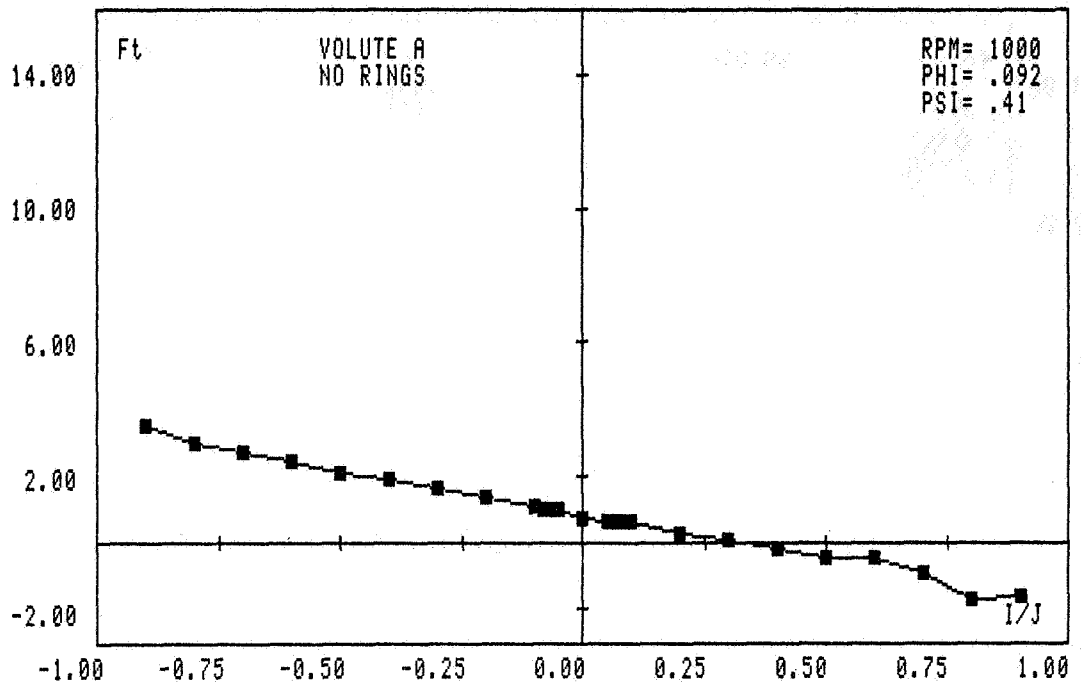

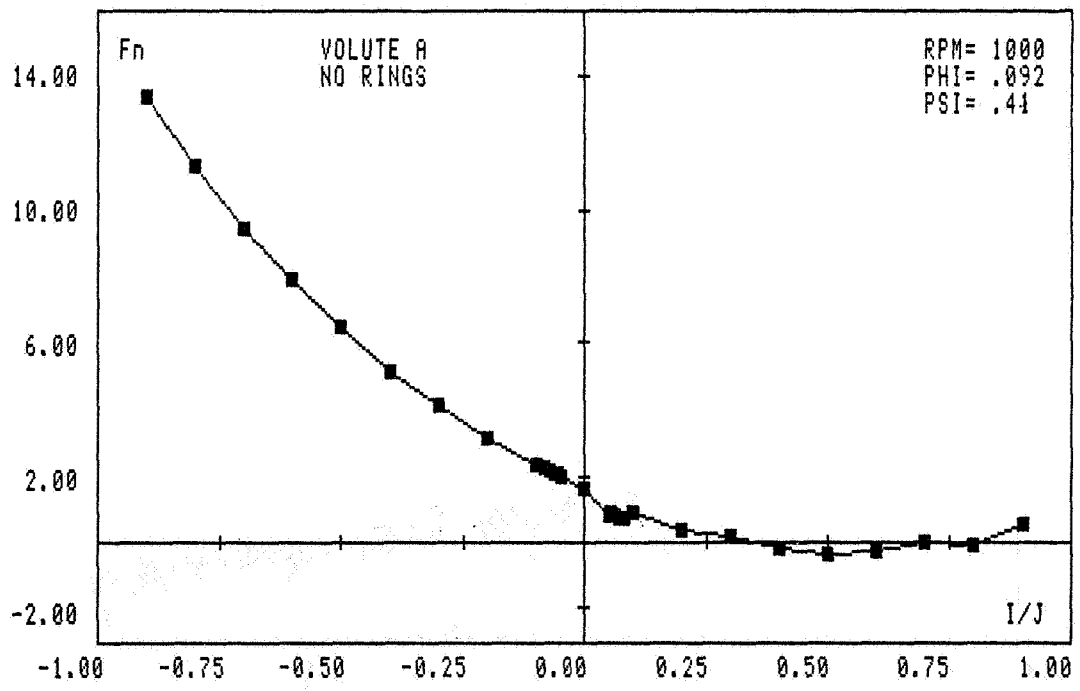

Figure 10. The dimensionless normal and tangential forces, F_N, F_T corresponding to Figure 9.

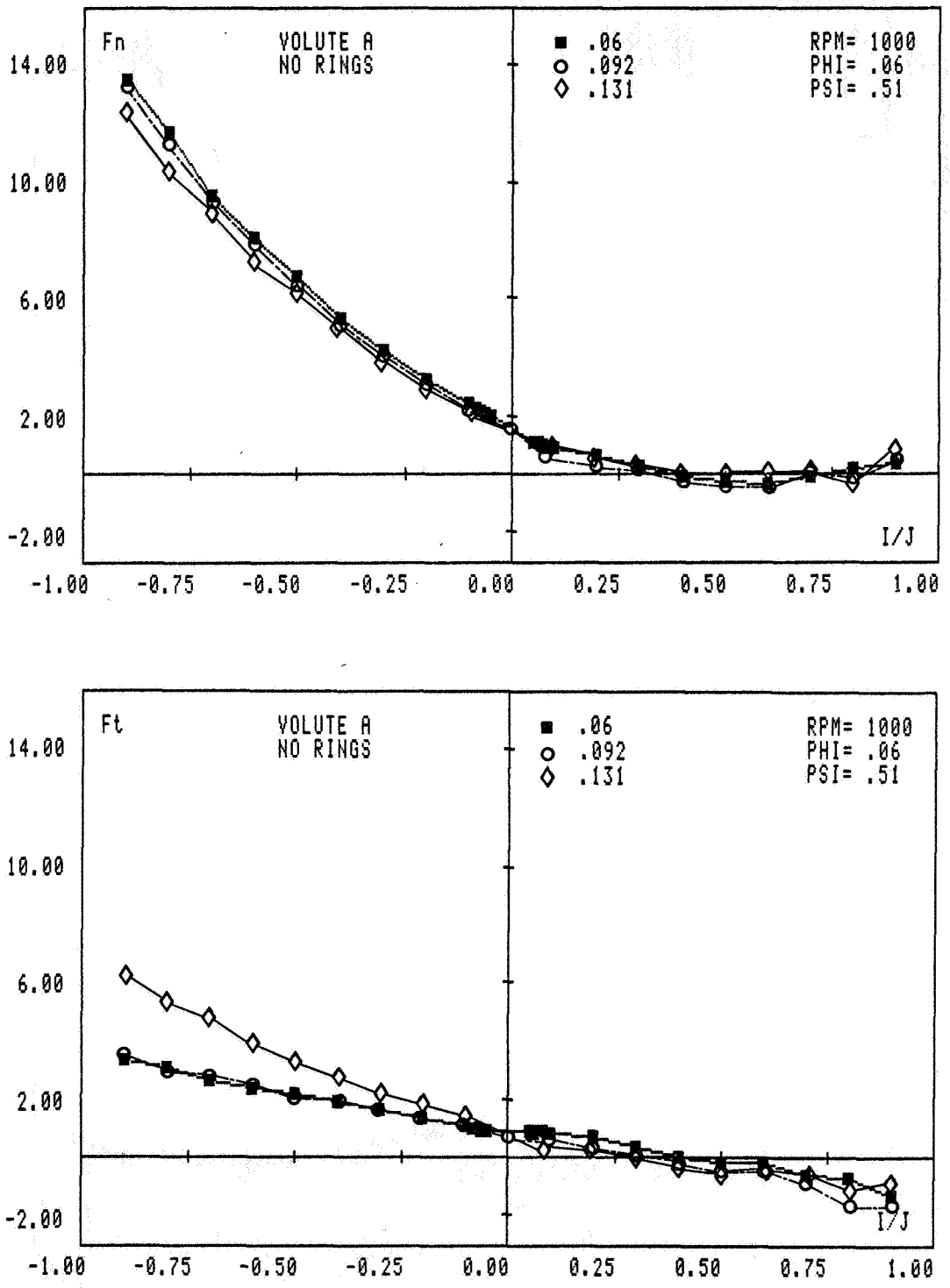

Figure 11. The normal and tangential forces for Volute A/Impeller X at 1000 rpm for three flow coefficients ϕ = 0.06, 0.092, 0.131.

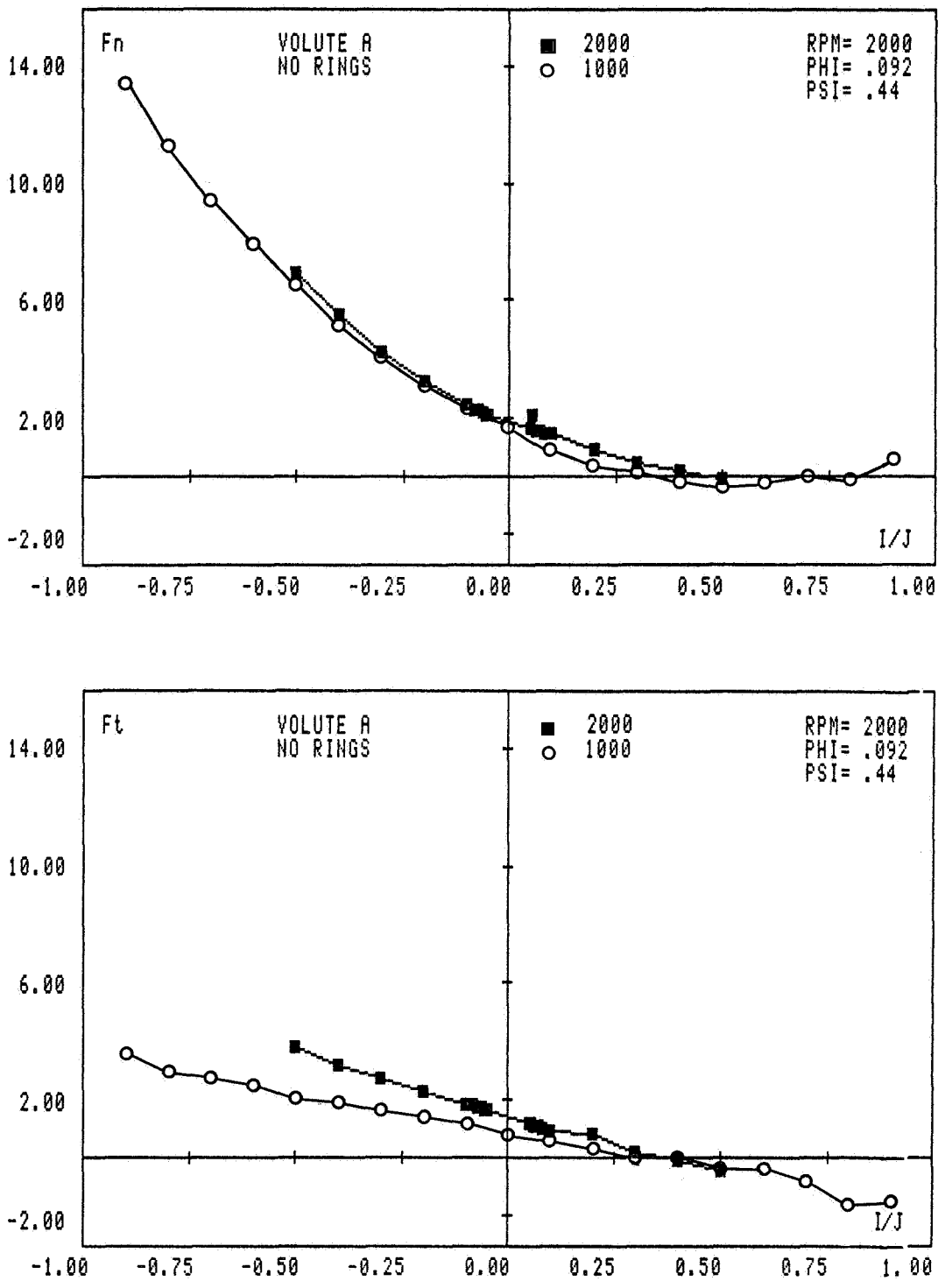

Figure 12. The normal and tangential forces, for Volute A/Impeller X at the design flow coefficient ϕ = 0.092 and two different pump speeds, 1000 rpm and 2000 rpm.

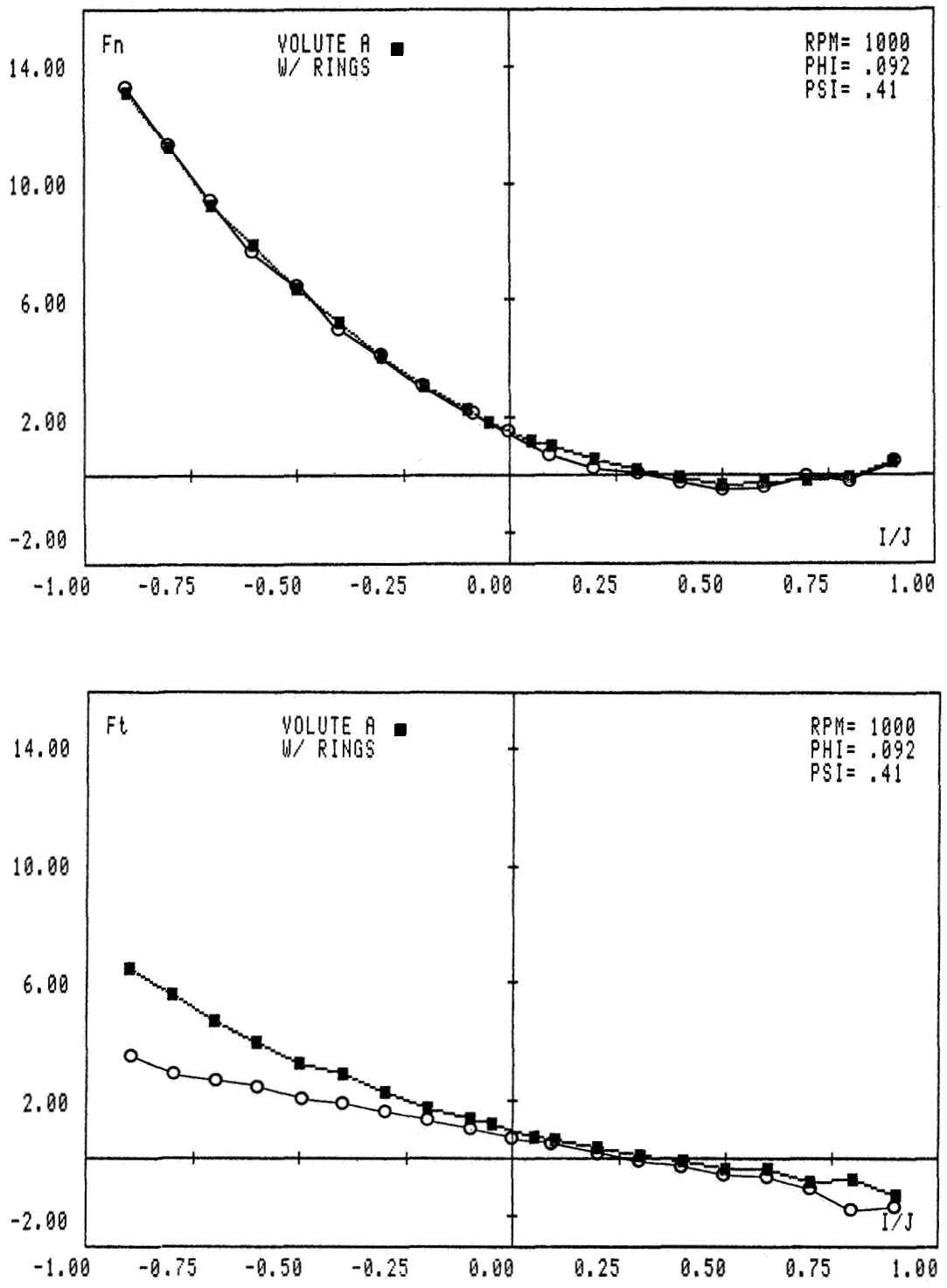

Figure 13. The normal and tangential forces F_N, F_T for Volute A/Impeller X at 1000 rpm and the design flow coefficient, $\phi = 0.092$ showing the effect of the leakage limiting rings.

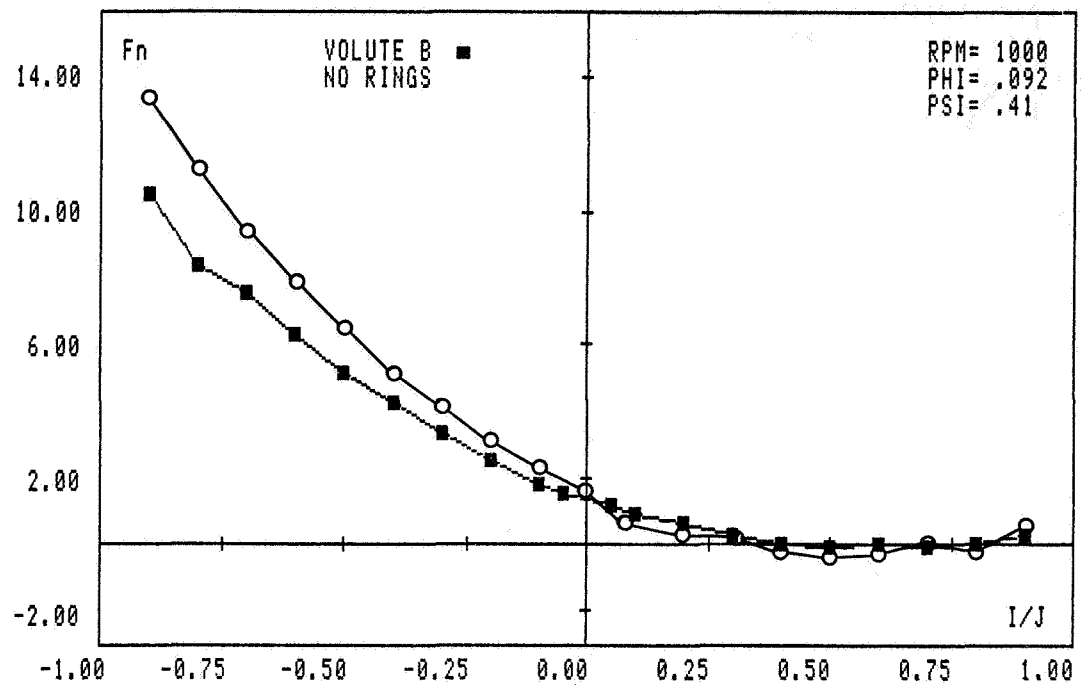

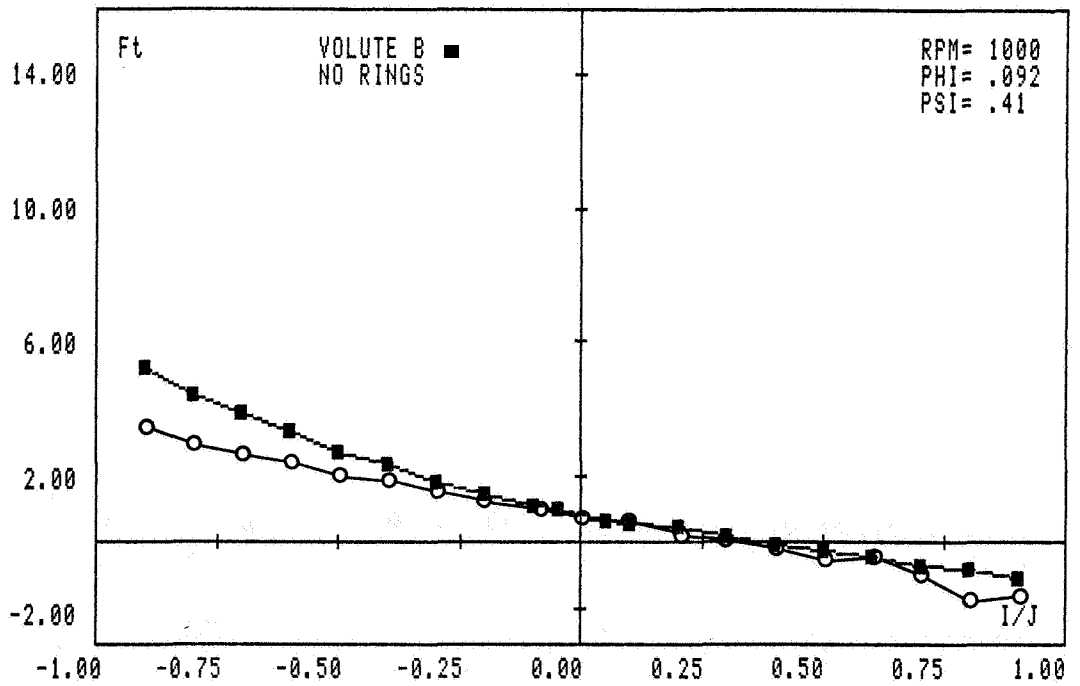

Figure 14. Comparison of F_N, F_T for Volutes A and B at 1000 rpm and ϕ = 0.092.

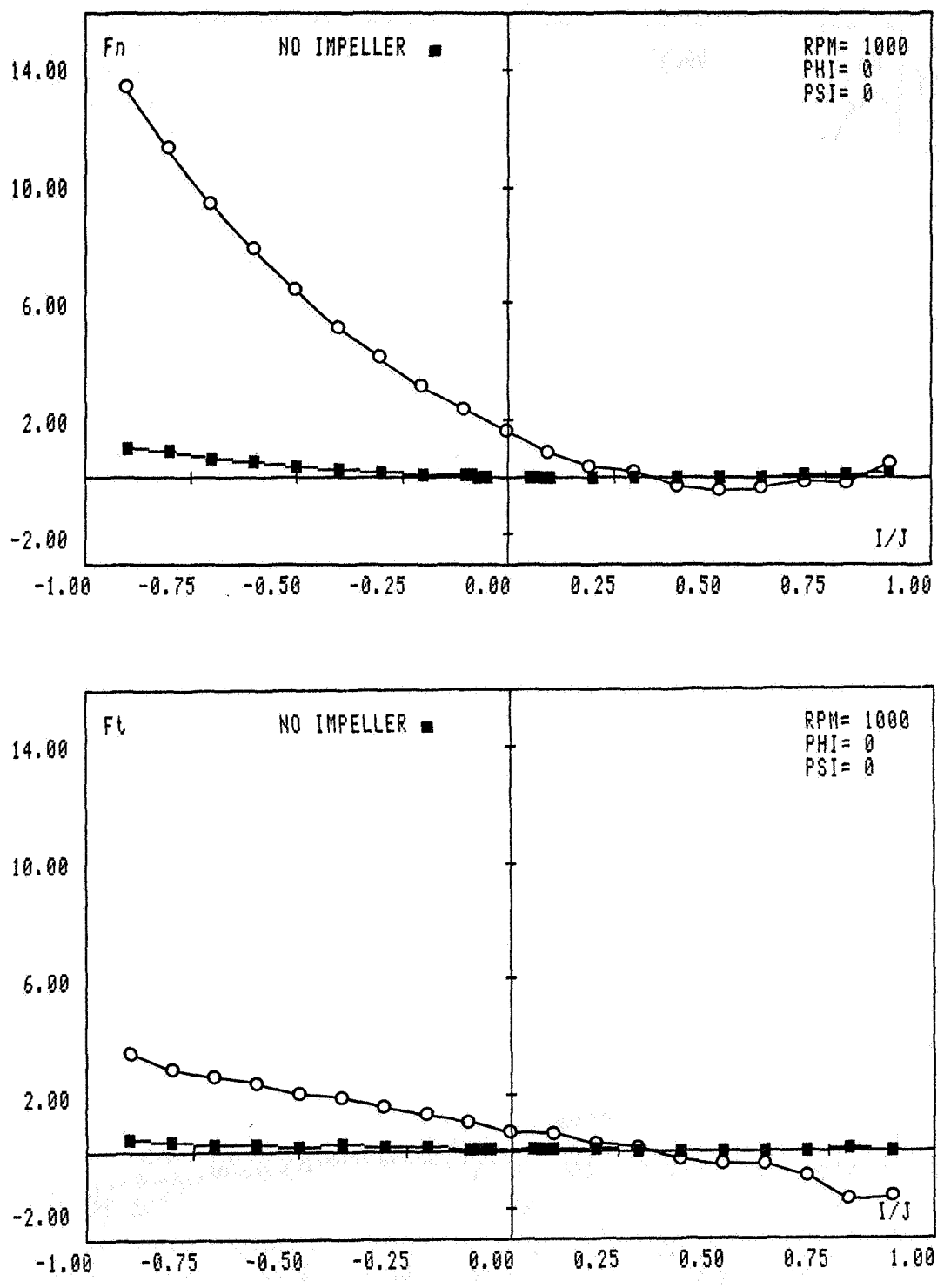

Figure 15. **The hydrodynamic tare effect of the internal balance when tested without an impeller at 1000 rpm.**